Received: 17 April 2023 | Revised: 14 June 2023 | Accepted: 18 June 2023

DOI: 10.1111/jace.19313

Journal of the American Ceramic Society

RESEARCH ARTICLE

Effect of Ti-metal addition on hot-isostatically pressed (HIPed) Synroc-C

Rifat Farzana[1] | **Pranesh Dayal**[1] | **Anton Peristyy**[1] | **Phillip Sutton**[1] | **Zaynab Aly**[1] | **Robert D. Aughterson**[1] | **Thanh Ha Nguyen**[1] | **Michelle Yeoh**[1,2] | **Pramod Koshy**[2] | **Daniel J. Gregg**[1]

[1]Australian Nuclear Science and Technology Organisation, Kirrawee DC, New South Wales, Australia

[2]School of Materials Science and Engineering, UNSW Sydney, Sydney, New South Wales, Australia

Correspondence
Daniel J. Gregg, Australian Nuclear Science and Technology Organisation, Locked Bag 2001, Kirrawee DC, NSW, Australia.
Email: dgg@ansto.gov.au

Abstract

Synroc, a candidate nuclear wasteform and Synroc technology, a waste treatment solution utilizing hot-isostatic pressing (HIPing) have significant potential for the immobilisation of challenging nuclear wastes from both current and innovative reactors and fuel cycles. Hot isostatic press (HIP) consolidation is undertaken within sealed metal HIP canisters, where metal buffers (e.g., Ti, Fe and Ni) can be incorporated to control the redox environment within the canister. This study, for the first time, reports the effect of varying Ti-metal addition (0, 2, 4, and 8 wt.%) on phase formation, microstructural characteristics, and wasteform performance for HIP consolidated Synroc-C containing 20 wt.% simulated PUREX type (PW-4b) high level waste. Quantitative X-ray diffraction analysis, scanning electron microscopy-energy dispersive X-ray spectroscopy (EDS) and transmission electron microscopy-EDS analyses were undertaken for analytical investigations. The chemical durability of the samples was assessed using ASTM C1220-21 standard test. Hot-isostatically pressed (HIPed) samples with 0 and 8 wt.% Ti added for redox control produced unfavourable phase formation. However, the HIPed samples with Ti additions of 2 and 4 wt.% as a redox buffer showed the desired phase formation of Synroc-C without any significant change to the partitioning of waste elements among the phases along with compatible durability results, when compared to previous literature for hot uniaxial pressing (HUPed) or sintered materials.

KEYWORDS

hot isostatic press (HIP), redox control, Synroc technology, Synroc-C, Ti-addition, wasteform

1 | INTRODUCTION

Synroc (Synthetic rock) is a multiphase ceramic wasteform pioneered in 1978 by Ringwood's team[1] in Australia. Synroc technology at Australian Nuclear Science and Technology Organisation (ANSTO) is a waste treatment solution that utilises hot isostatic pressing (HIPing) to produce glass, glass-ceramic and ceramic wasteforms for the immobilisation of challenging nuclear wastes.[2] The class of wasteform and its design is tailored to the

chemical, physical and radiological characteristics of the waste and to meet the performance requirements for storage and disposal. The technology provides an opportunity to treat nuclear wastes that are problematic for glass matrices alone or existing vitrification technology, such as actinide-bearing wastes,[3,4] wastes with significant corrosive or fission product volatile emissions,[5,6] or wastes with substantial refractory components.[2] The technology is maturing towards the treatment of ANSTO's radiopharmaceutical production intermediate-level liquid waste through the construction of a first-of-a-kind Synroc Waste Treatment Facility at ANSTO.[2]

Synroc-C (C for commercial nuclear power fuel waste) was one of the first Synroc formulations,[1,3] and this is a multiphase, thermodynamically stable polycrystalline titanate mineral assemblage consisting of mainly, Ba-hollandite (nominally $BaAl_2Ti_6O_{16}$), zirconolite (nominally $CaZrTi_2O_7$), and perovskite (nominally $CaTiO_3$). Synroc-C is a unique variation of Synroc designed specifically for the immobilisation of commercial PUREX type waste or simulated high level waste (HLW).[7] It was demonstrated to have enhanced aqueous durability relative to borosilicate glass wasteforms in short-term standard test methods and is therefore expected to function as an improved barrier to the release of radionuclides into the biosphere relative to nuclear waste glasses.[8] In combination, the titanate minerals of Synroc-C have the ability to incorporate the elements present in HLW such as actinides U, Np, Pu, rare earth elements La, Y, noble metals, and fission products (e.g., Sr, Mo, Cs, Ba etc.). The waste elements are incorporated into the titanate crystal structures at regular lattice sites in the form of dilute solid solutions or as an alloy phase.

Synroc-C accommodates PW-4b type reprocessing waste at a range of ~5–35 wt.% with the standard Synroc-C designed to contain approximately 20 wt.% simulated commercial waste.[4] The phase assemblage of Synroc-C incorporating 20 wt.% waste consisted of approximately 30 wt.% hollandite, 30 wt.% zirconolite, 20 wt.% perovskite, 15 wt.% rutile and/ or Ca-Al titanate, and 5 wt.% alloys or phosphate phases and was produced by cold pressing and sintering or hot uniaxial pressing (HUPing) consolidation.[3] The hollandite crystal structure has the general formula $A_xB_yC_{8-y}O_{16}$, $x \leq 2$, where A is the large monovalent or divalent cation (tunnel cations) and B and C represent di-, tri-, tetra- and penta-valent cations. B cations are generally lower valence than C cations and $(B,C)O_6$ octahedra are linked together by edge-sharing to form a double chain running parallel to the *c*-axis for tetragonal phases or the *b*-axis for the monoclinic hollandite structure.[3] The titanate hollandite of Synroc-C is comprised of Cs, Ba, and minor Rb as tunnel cations and Al or Ti as trivalent species.[3] Zirconolite ($CaZr_xTi_{3-x}O_7$, $0.8 < x < 1.37$) has the ability to incorporate U, tetravalent actinides and to a lesser extent rare earth elements (REE) and trivalent actinides.[3] Ca is coordinated by 8 oxygen ions positioned at the corners of a cube while Zr is in sevenfold coordination to oxygen at seven of the eight vertices of a distorted cube. Ti occupies three distinct lattice sites, in Ti(I) and Ti(III) positions and is octahedrally coordinated to 6 oxygen ions, and these TiO_6 octahedra are corner linked forming six- or three-membered rings respectively. The Ti(II) site is half occupied and surrounded by 5 oxygen ions at the corners of a trigonal bipyramid.[3,9,10] The ideal zirconolite is comprised of planes of corner and edge sharing CaO_8 and ZrO_7 polyhedra, interleaved by hexagonal tungsten bronze (HTB) type Ti–O layers along (001) and is referred to as zirconolite-2M. The zirconolite polytypes (2M, 3T, 4M) are then characterized by the variation in a stacking sequence of adjacent Ca/Zr and HTB-type Ti–O layers.[3] Perovskite ($CaTiO_3$) in Synroc-C is the primary host for Sr, trivalent actinides, REE and Na. The large cations (Ca^{2+}) are centrally located in the twelvefold coordinated positions between groups of four TiO_6 octahedra and the small cations (Ti^{4+}) are surrounded by oxygen ions forming the octahedral, which are linked by corner sharing.[3,9] Rutile (TiO_2) phase formation is dependent on redox conditions. The production of Synroc-C involved the addition of TiO_2, ZrO_2, CaO, BaO and Al_2O_3 as precursors with the PUREX type HLW as well as additional Ti metal powder. Without Ti addition, Synroc-C contains abundant rutile however, with Ti metal addition and/or exceptionally reducing conditions, rutile is rarely observed and several Magnéli phases are evident.[3] In nature also, Ti^{4+} is prevalent but under particular conditions it undergoes reduction to Ti^{3+} and forms Magnéli (Ti_nO_{2n-1}) phases.[11] These Magnéli phases are nonstoichiometric titanium oxides comprised of a series of distinct compounds with the generic formula Ti_nO_{2n-1}, where "n" is an integer between 3 and 10 (and more typically between 4 and 6).[12,13] These phases contain an increasing amount of Ti^{3+} with decreasing "n" values.[11] It is evident that atom substitution mechanisms along with structural modifications of the Synroc-C phase assemblage provide the ability for the system to accommodate a diverse range of cationic charge and ionic radii.[3] Also, Synroc-C allows minor but spontaneous phase assemblage adjustments over the waste-stream compositional variations.[3]

The effect of impurities, including metal additives such as Ni and Ti on Synroc-C samples (hot pressed in graphite die) with 10 wt.% waste loading have been studied to understand the controlling parameters of element partitioning.[14] Overall, the presence of "excess TiO_2" and the supply of Ti^{3+} (by addition of Ti metal to react with TiO_2) in the formulation were pivotal to the incorporation of waste species into the Synroc phase assemblage, other

than noble metals.[3,15] In a separate study, Ryerson[16] also observed an abrupt change in phase assemblage of Synroc-D, the titanosilicate variation established for defence waste, due to oxygen fugacity variations. Maintaining the appropriate reducing conditions during consolidation by adding Ti metal is also crucial, as it influences the final elemental distribution. The reducing conditions serve to prevent the formation of soluble caesium molybdate and allow Cs to enter the hollandite structure and consequently promote Cs immobilisation.[3,15] Moreover, it is essential to create a sufficiently reducing environment to stabilize Mo, Ru, Te, and Tc from the HLW in the metallic state. The exothermic nature of Ti oxidation is also beneficial to grain growth of the TiO_x relics containing elements such as Al, Ca, Fe etc. that have diffused into this structure.[3]

Several processing methods have been employed for the consolidation of Synroc-C type ceramics, including conventional sintering, joule/cold crucible melting, HUPing, HIPing and spark plasma sintering (SPS). Conventional or pressure-less sintering was adopted as the consolidation method for Synroc-C in the late 1970s to early 1980s.[17] Later, HUPing in graphite dies or small steel bellows[17,18] appeared to be an attractive alternative, primarily for operational simplicity and radiological contamination minimisation. In addition, HUPed wasteforms showed an increase in wasteform density, reduction in monolith size and reduced loss of volatile components/radioactive dust during hot pressing.[17,18] The graphite dies used for the HUP process provided sufficiently reducing conditions through CO generation, nevertheless, chances of contamination from the dies existed. Although HUPing in the steel bellows allows larger scale wasteform production, HIPing in a custom designed canister, enables safer operation, faster turnover without compromising wasteform size, enhanced wasteform properties such as higher density, improved mechanical strength and no volatile losses.[2] Early in the 2000s, ANSTO adopted HIPing as the preferred consolidation process due to its advantages over other technologies and transitioned into the Synroc technology platform using HIPing.[2]

The microstructural characteristics, durability and physical properties of Synroc-C were previously studied as a function of temperature and consolidation method, including cold press and sinter, HUP, HIP, and SPS.[19] It was observed that HUPed (1150 - 1250°C under 20 MPa) and Hot-isostatically pressed (HIPed) (1200°C under 100 MPa) Synroc-C samples showed a high quality microstructure and leach resistance compared to pressure-less sintered samples.[19] SPS samples (1100°C under 50 MPa) showed high density and a fine grained microstructure but the partitioning of Mo into a stable metallic state was not observed.[19,20]

Synroc-C was originally produced with 2 wt.% of Ti metal fine powder added to reduce the redox potential during HUP processing.[3] However, Ti metal addition during HIP consolidation of Synroc-C has not been examined or optimised, nor has the impact of varying amounts of Ti metal additions to the phase evolution, microstructural characteristics and durability properties been established. In the current study, dense, compact Synroc-C samples, containing 20 wt.% simulated PUREX type (PW-4b) high level waste were prepared under the same consolidation conditions with varying Ti metal additions (0, 2, 4, and 8 wt.%) to control the redox state within the HIP canister and subsequently the oxidation state of the multivalent cations. All samples were produced via HIPing at ANSTO, and were characterized using X-ray diffraction (XRD), scanning electron microscopy (SEM), and transmission electron microscopy (TEM) analyses to establish the phase formation and elemental distribution in the samples. Aqueous durability studies were conducted using the standard test method ASTM C1220. Performance in these short-term durability tests was compared to Synroc-C produced via HUP processing and results are discussed in the context of Ti metal addition, phase formation and microstructural characteristics.

2 | EXPERIMENTAL

2.1 | Materials and method

The Synroc-C samples were synthesized by a modified nitrate/alkoxide chemical route. All chemicals were analytical reagent grade (Sigma-Aldrich) and used as received. Samples of ~200 g were prepared (oxide basis) and the simulated waste components were included such that they made up 20 wt.% (oxide basis) of the final composition. Aqueous mixtures of stoichiometric amounts of metal nitrate solutions of $Al(NO_3)_3.9H_2O$, $Ba(NO_3)_2$, $Ca(NO_3)_2.4H_2O$, $CsNO_3$, $Sr(NO_3)_2$, $Ru(NO)(NO_3)_3$, $Gd(NO_3)_3.6H_2O$, $Nd(NO_3)_3.6H_2O$, $Ce(NO_3)_3.6H_2O$, $AgNO_3$, $Pd(NO_3)_2.2H_2O$, $Cr(NO_3)_3.9H_2O$, $Fe(NO_3)_3.9H_2O$, $Ni(NO_3)_2.6H_2O$, $Y(NO_3)_3.6H_2O$, $(NH_3)_6Mo_7O_{24}.4H_2O$ and titanium isopropoxide (TiPt), and tetrabutyl zirconate (TBZ) were stirred at room temperature in a stainless-steel beaker for 4 h.

The mixture was then heated until drying occured while stirring on a hot plate at ~110°C. The dried powder was subsequently calcined under flowing N_2-3.5%H_2 for 6 h at 750°C in a rotary furnace. The calcined powder was then milled using yttria-stabilized zirconia balls in cyclohexane for 16 h and dried at ~110°C. Ti metal powder (325 mesh, 99.5% purity) was added at levels of 0, 2, 4, and 8 wt.% to the calcined material, to investigate the effect of

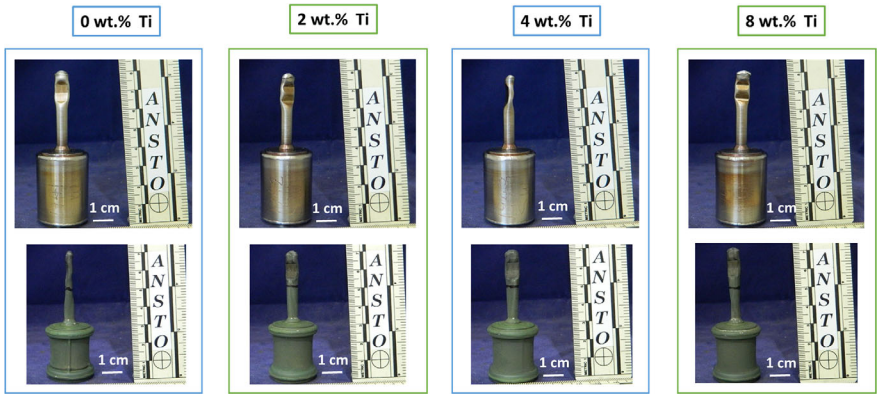

FIGURE 1 Hot isostatic press (HIP) canisters before (top row) and after (bottom row) HIPing with varying Ti-metal addition.

TABLE 1 Composition of precursor oxides and waste oxides before Ti addition.

Oxides	Name	Weight %
Precursor oxides (80 wt.%)	TiO_2	57.0
	ZrO_2	5.4
	Al_2O_3	4.3
	BaO	4.4
	CaO	8.9
Waste oxides (20 wt.%)	Fe_2O_3	3.82
	Cs_2O	8.26
	SrO	2.68
	BaO	3.93
	Y_2O_3	1.55
	ZrO_2	12.5
	MoO_3	13.12
	RuO_2	7.54
	PdO	3.72
	CeO_2	12.19
	Nd_2O_3	15.5
	Gd_2O_3	3.72
	U (ZrO_2)*	5.16
	Cr_2O_3 + NiO + Ag_2O	2.59

*Additional ZrO_2 was added as a substitute for UO_2.

Ti addition and the sample identifications are: 0 wt.% Ti, 2 wt.% Ti, 4 wt.% Ti and 8 wt.% Ti respectively. The blended powders were then HIPed in stainless steel (SS) HIP canisters at 1250°C with 100 MPa pressure for 2 h. The oxide compositions of the samples along with PUREX type HLW simulated waste is given in Table 1 and the HIPed canisters before and after HIPing are shown in Figure 1.

2.2 | Analytical techniques

XRD was conducted by a PANalytical X'Pert Pro diffractometer (Almelo, the Netherlands) with Cu-Kα radiation ($\lambda = 1.54$ Å) at 40 kV and 45 mA, in the range $10° < 2\theta < 80°$, with a step size of 0.02° (2θ). X'pert highscore plus phase identification software was used to identify the Synroc-C phases. The Rietveld refinement method was used for Quantitative phase analysis (QPA) using TOPAS v.5 software, and all the crystallographic information files were obtained from the inorganic crystal structure database.

Synroc-C phase morphology and composition were analyzed by SEM and energy dispersive X-ray spectroscopy (EDS). A Zeiss Ultra Plus instrument (Carl Zeiss NTS GmbH, Oberkochen, Germany) was used operating at an accelerating voltage of 15 kV and equipped with an Oxford Instruments Ultim Max 170 mm^2 SDD X-ray microanalysis system. All samples were prepared for SEM-EDS after mounting in epoxy resin, and polishing and coating with ~10 nm of carbon to avoid effects of charging.

TEM was carried out on a JEOL 2200FS microscope operated at 200 kV. This microscope is equipped with an Oxford X-Max EDS system with data analyzed via the Oxford INCA microanalysis software. The TEM was operated in standard TEM mode with bright field and high-resolution images captured via Gatan Orius and Ultra cameras respectively. Scanning TEM (STEM) was also used for collection of EDS maps. TEM specimens consisted of mechanically polished discs, approximately 3 mm wide by 80 microns thick at outer edges. Mechanical polishing was achieved via a Leica EM TXP cutting and polishing unit using various grades of diamond lapping foils down to 2 microns. A final polish to electron transparency was achieved via a Gatan precision ion polishing, model 691, system using 5 keV argon ions incident at 3–5° relative to the specimen surface.

Durability analysis was undertaken according to the standard test method *ASTM C1220-21 Standard Test Method for Static Leaching of Monolithic Waste Forms for Disposal of Radioactive Waste*,[21] using Reference Test Matrix B. Reference Test Matrix B can be used to compare the test responses of different waste forms and tests conducted with a material at different laboratories. The two largest faces of the tabular test specimens (69% of total surface area) were polished to a 1-μm diamond

finish, with the remaining faces (31% of total surface area) left unpolished (as cut). Cyclohexane was used as the washing fluid to remove adherent fines from the prepared samples due to concerns regarding the potential preferential aqueous solubility of separated phases. ASTM Type I deionised water (18.2 MΩ•cm) was employed as the leachant and was prepared immediately before use. The test conditions were a 28-day test duration, perfluoroalkoxy alkanes leach vessels, 90°C leach temperature and 10 m^{-1} test specimen surface area/leachant volume ratio. The test vessels were acid-stripped after leaching using 2% v/v nitric acid solution at 90°C for 12 h to recover species adhering to the interior surfaces of the test vessel. The unfiltered leachate and acid strip solutions were analyzed for elemental composition by inductively coupled plasma-mass spectrometry. Normalised elemental mass loss values were calculated using the elemental composition of the unaltered wasteform on an "as-batched" basis. Reported measurement uncertainties (95% confidence level) were estimated using the 'top-down' method for the evaluation of uncertainty for empirical methods, described in Sect. 7.9 of Eurachem/CITAC guide CG 4.[22]

Sample density and porosity were recorded using Archimedes' method in distilled water according to ISO 18754.

3 | RESULTS AND DISCUSSION

3.1 | Phase assemblage and structure of Synroc-C with Ti addition

The XRD patterns in the 2θ range of 10−80° for 0−8 wt.% Ti addition samples are shown in Figure 2. The targeted phase assemblage of Synroc-C was identified for the 0, 2 and 4 wt.% Ti samples. Distinct peaks of hollandite (PDF: 01-084-0509, space group $I4/m$), zirconolite (PDF: 01-034-0167, space group $C2/c$), and perovskite (PDF: 01-077-0182, space group $P2_1/m$) were observed for these samples. Rutile (PDF: 01-088-1173, space group $P4_2/mnm$) peaks were evident in the XRD patterns for the 0 and 2 wt.% Ti samples, with relatively lower peak intensities for the 2 wt.% Ti sample. Peaks for the Magnéli phase of Ti_3O_5 were evident in the XRD pattern for the 4 wt.% Ti sample at around $2\theta = 25°$, while no rutile peaks were observed. In addition, with increasing Ti-metal for the 0, 2, and 4 wt.% samples, there appears to be a decrease in peak intensity for the hollandite and zirconolite phases relative to the perovskite phase. The sample with 8 wt.% Ti shows complete absence of hollandite and zirconolite phases as evidenced by the loss of diffraction intensity for the main zirconolite ($2\theta = 30.8°, 50.7°, 53.0°$) and hollandite ($2\theta = 28.0°, 36.6°$) reflections in the XRD pattern. Perovskite remains as the

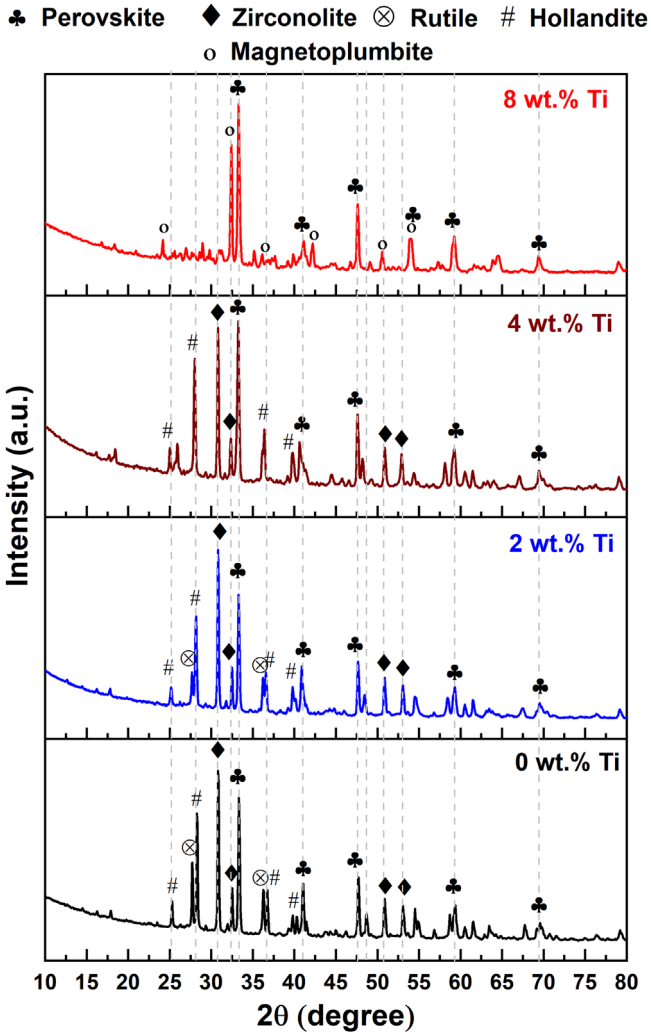

FIGURE 2 X-ray diffraction (XRD) patterns showing major peaks for the hollandite, zirconolite, perovskite, rutile, and magnetoplumbite-type phase assemblage in the HIPed Synroc-C sample with 0−8 wt.% Ti addition.

predominant original Synroc-C titanate phase with a new major peak in the XRD pattern at $2\theta = 32.3°$ indicating the presence of magnetoplumbite-type phase (PDF: 01-072-0738, space group $P6_3/mmc$). Magnetoplumbite phases were reported previously with Synroc-C phases under highly reducing conditions.[23] Further, the low intensity peaks at $2\theta = 26.6°, 29.7°, 36.2°$ in the XRD pattern for the 8 wt.% Ti sample are consistent with the presence of loveringite (PDF: 00-042-1368). However, unequivocal phase identification for these low intensity peaks for this sample was challenging given the wide range of phases possible via solid solutions within the CaO-Al_2O_3-ZrO_2-TiO_2 and BaO-TiO_2-Al_2O_3 systems. To support assignments, the chemistry of phases present in the sample with 8 wt.% Ti was defined where possible using the elemental analysis from TEM-EDS analysis (Table 4, Table S2).

TABLE 2 Semi-quantitative analysis of X-ray diffraction (XRD) data showing the phase assemblage wt.% of Synroc-C with 20 wt.% waste oxides incorporated.

Sample name	Phases				
	Hollandite	Zirconolite	Perovskite	Rutile	Magnéli
Ringwood's Synroc-C[3]					
Synroc-C	30	30	20	15	
Present work					
0 wt.% Ti	31.1 ± 0.3	29.8 ± 0.3	26.8 ± 0.3	12.3 ± 0.2	–
2 wt.% Ti	36.0 ± 0.5	31.3 ± 0.4	25.7 ± 0.3	7.0 ± 0.4	
4 wt.% Ti	31.7 ± 0.4	24.9 ± 0.4	27.9 ± 0.4	–	15.4 ± 0.6

TABLE 3 Unit cell parameters of the hollandite phase with 0–4 wt.% Ti addition.

Lattice Parameter (nm)	Reference	0 wt.% Ti	2 wt.% Ti	4 wt.% Ti
a	9.982	10.0638 (5)	10.1052 (9)	10.1518 (9)
c	2.933	2.9394 (2)	2.9509 (4)	2.9649 (4)

The addition of Ti metal likely enhanced the formation of Ti^{3+}, which appears to destabilize the zirconolite and hollandite phases in comparison to perovskite to the point at which these phases are no longer formed as part of the phase assemblage. This is clearly evident in the case of the addition of 8 wt.% Ti metal. This behavior is consistent with the literature where enhanced formation of perovskite in relation to zirconolite has been observed previously for actinide-doped zirconolites annealed in reducing conditions.[24] The pyrochlore structure, which is a close structural relative of zirconolite, was shown to be similarly destabilized relative to perovskite and UO_2 under near identical reducing conditions within a HIP canister in a recent study investigating pyrochlore glass-ceramics produced via HIP consolidation.[25]

Semi-QPA of the XRD data was conducted using TOPAS software, and the results are summarized in Table 2. Representative data are shown in Figure S1. The percentages of the different phases match closely with the phase assemblage in Ringwood's original Synroc-C incorporating 20 wt.% (PW-4b) waste loading.[3] The semi-QPA also confirms the formation of Ti^{3+} due to Ti metal addition. The amount of Ti_3O_5 (PDF: 01-089-4733, space group *Cmcm*) was significant in the 4 wt.% Ti sample with the peaks at 2θ values of ~18 and 25° (Figures 2 and 3) representing the (0 2 0) and (1 1 0) planes of Ti_3O_5, respectively. The few unassigned peaks, such as those seen at 2θ: 26.69° and 34.74° are attributed to metal alloy or other Magnéli phases.

A distinct peak shift toward lower angle (Figure 3) was also observed for hollandite in the XRD pattern for 0–4 wt.% Ti samples. This is indicative of an increase of the unit cell parameters for hollandite. The corresponding lattice parameter changes of the hollandite phase are tabulated in Table 3. The *a* and *c* unit cell parameters were observed to increase with increasing Ti addition, indicating that Ti addition, results in cationic substitution of the hollandite phase. This is evident from a significant reduction of Al content in the hollandite grains (Table 4) for the sample with 4 wt.% Ti, which is likely facilitated by the reducing conditions, which enhances the formation of Ti^{3+}. Substitution of Al^{3+} with the larger Ti^{3+} cation is therefore responsible for the systematic shift of the peaks in the hollandite XRD pattern to lower angles with increasing Ti metal addition. Similar shifts were not observed for the zirconolite or perovskite phases and cell parameters showed only minor changes.

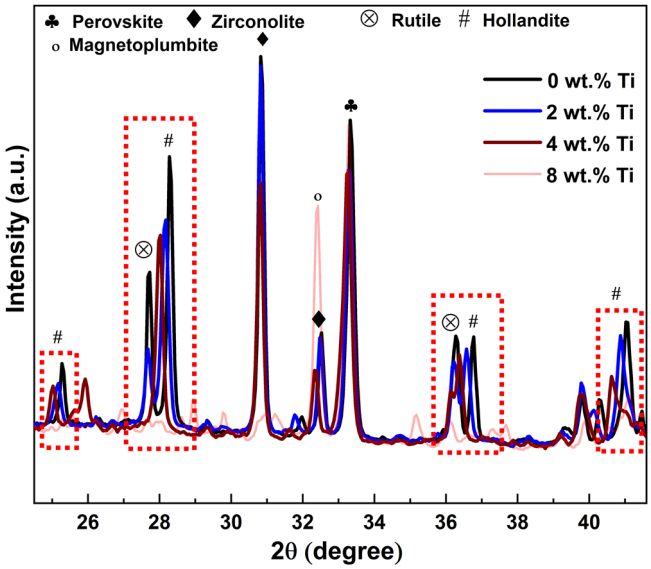

FIGURE 3 X-ray diffraction (XRD) patterns showing the peak shift of the hollandite phase to lower angle with increasing Ti metal addition.

TABLE 4 Phase compositions for hollandite, zirconolite, and perovskite (the Synroc-C phases) with varying Ti metal addition as determined from transmission electron microscopy (TEM)-energy dispersive X-ray spectroscopy (EDS) analyses.

Phase	Ti addition (wt.% Ti)	Phase composition[1]
Hollandite[2]	0	$(Ba_{1.1}Ca_{0.05}Cs_{0.05}Sr_{0.02})(Al_{1.25}Cr_{0.05}Fe_{0.2}Mo_{0.2}Ti_{6.25})O_{16}$
	4	$(Ba_{1.0}Ca_{0.1}Cs_{0.2}Sr_{0.03})(Al_{0.55}Mo_{0.25}Zr_{0.1}Ti_{7.0})O_{16}$
	8	Not present
Zirconolite[3]	0	$(Ca_{0.7}Ce_{0.05}Gd_{0.05}Nd_{0.1}Y_{0.05})Zr_{0.9}(Ti_{1.95}Al_{0.2}Fe_{0.05})O_7$
	4	$(Ca_{0.7}Ce_{0.05}Gd_{0.05}Nd_{0.1}Y_{0.05})Zr_{0.95}(Ti_{1.9}Al_{0.25})O_7$
	8	Not present
Perovskite[4]	0	$(Ca_{0.7}Ce_{0.1}Sr_{0.05}Nd_{0.05})(Ti_{0.95}Al_{0.05})O_3$
	4	$(Ca_{0.7}Ce_{0.1}Sr_{0.02}Nd_{0.05})(Ti_{0.9}Al_{0.05}Mo_{0.02})O_3$
	8	$(Ca_{0.7}Ce_{0.05}Sr_{0.02}Nd_{0.05})(Ti_{0.9}Al_{0.05}Zr_{0.05}Mo_{0.02})O_3$

[1]Oxygen content was not measured, [2]assuming a total of eight cations on the Al- and Ti-sites, [3]assuming a total of four cations on the Ca-, Zr-, and Ti-sites, [4]assuming a Ti-site occupancy of 1.

3.2 | Phase composition and microstructure of Synroc-C with Ti addition

The morphology of the samples is shown through low and high magnification SEM images in Figure 4. Overall, the samples did not show any evidence of unreacted Ti metal which indicates that all the Ti was consumed (by scavenging excess oxygen and subsequent chemical reaction with neighbouring compounds or phases) during the HIPing process. Rutile or Magnéli (Ti_nO_{2n-1}) phases were identified through their darker contrast, and these were seen to be dispersed throughout the sample. These oxides are collectively termed Ti-oxide relics (TiO_x) and were evident in all samples. However, it was observed that Ti_nO_{2n-1} was predominant for the 8 wt.% Ti sample compared to rutile. Acicular crystals and irregular crystals were both found to be present in the 2–4 wt.% Ti samples (shown in high magnification SEM images in Figure 4E-H). The acicular crystals were determined to be TiO_x with Ca and Al incorporated, while the irregular crystals were determined to be TiO_2/ Ti_nO_{2n-1} with minor amounts of Al incorporated. With increasing amounts of Ti^{3+}, Magnéli phases became predominant as was seen for the 2 and 4 wt.% Ti samples and these results are consistent with the XRD data. The abundance of relic phases (TiO_2/Ti_nO_{2n-1}) in HIPed and HUPed Synroc-C with 2 wt.% Ti added was previously determined to be ~20 wt.% at lower temperature (1150°C) and found to decrease to ~10 wt.% with increasing temperature (1325°C)[3,19] and is in agreement with the current study. For the highest Ti metal added sample (8 wt.% Ti), increased amounts of Ti-oxide relics were expected to have been observed. However, the additional Ti metal and subsequent formation of Ti^{3+}, appears to have resulted in the formation of new phases, with some remaining Ti-oxide relics also evident. SEM analysis (Figure 4E-H) clearly showed a multiphase assemblage for all samples studied, in agreement with the XRD analysis. Aside from the Ti-oxide relics and metal alloys, however, the elemental composition for the individual phases could not be accurately determined using SEM-EDS analysis due to the small sub-micron grain sizes. Therefore, a detailed phase identification and phase composition required TEM-EDS analysis and is discussed below. Based on the results from XRD and TEM-EDS analyses together with information from SEM-EDS analysis, the identity of the phases in the SEM are allocated where possible in Figure 4.

The high-magnification SEM images (Figure 4E-H) showed that some micron size pores exist for the 0 wt.% Ti sample, but the other samples showed a dense structure with almost no pores. The pores in the 0 wt.% Ti sample are attributed to the trapped gas bubbles (e.g., excess oxygen) due to the absence of Ti metal to scavenge gases. The resulting consolidated pellet showed a low-density value of 4.22 g/cm^3. For comparison, the density value for the 4 wt.% Ti sample was 4.41 g/cm^3 while the bulk densities for the SPSed and sintered Synroc-C samples without Ti,[26] were previously reported as 4.62 and 4.07 g/cm^3 respectively.

TEM-EDS analysis also confirmed the dense matrix as a multiphase Synroc-C ceramic assemblage of zirconolite (Z), barium hollandite (H), perovskite (P), and titanium oxide for 0–4 wt.% Ti samples with significant changes to the phase assemblage for the 8 wt.% Ti sample (Figure 5). Table 4 provides the elemental compositions of the targeted Synroc-C titanate phases to allow a detailed comparison of these common phases across the range of Ti addition. Elemental compositions of the non-Synroc phases present in the 8 wt.% Ti sample have been included in Table S2. The nominal phase composition of Synroc-C phase assemblage for the sample with 4 wt.% Ti metal addition was determined from TEM elemental analysis to be the following:

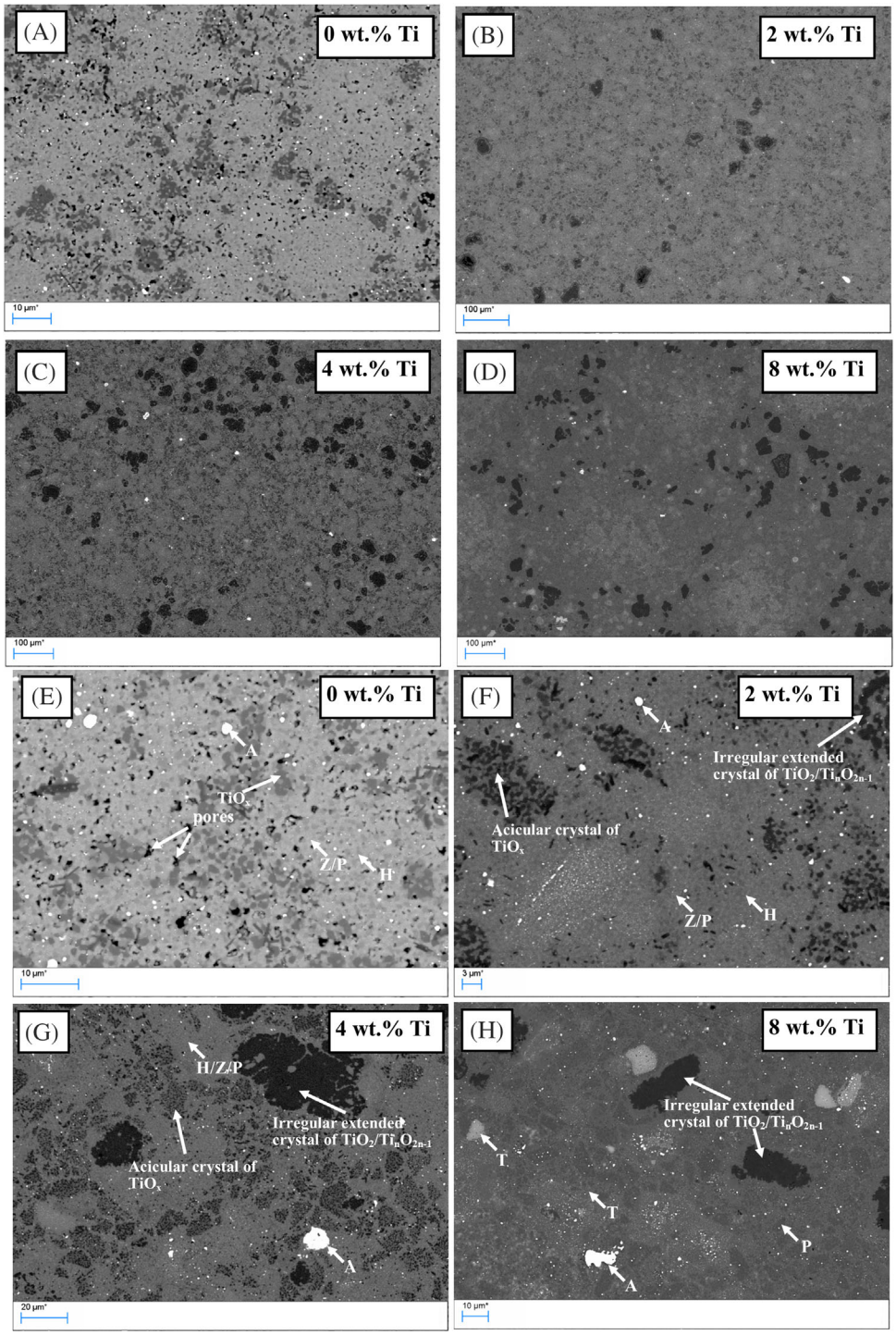

FIGURE 4 Backscattered scanning electron microscopy (SEM) images showing the morphology of the Synroc-C wasteform with 0, 2, 4, and 8 wt.% Ti additions. (A–D) showing the low magnification images and (E–H) high magnification images showing pores and the various phases (Z: zirconolite, H: hollandite, P: perovskite, A: metal alloy, T: magnetoplumbite-type or other phases.

Hollandite: $(Ba_{1.0}Ca_{0.1}Cs_{0.2}Sr_{0.03})(Al_{0.55}Mo_{0.25}Zr_{0.1}Ti_{7.0})O_{16}$

Zirconolite: $(Ca_{0.7}Ce_{0.05}Gd_{0.05}Nd_{0.1}Y_{0.05})Zr_{0.95}(Ti_{1.9}Al_{0.25})O_7$

Perovskite: $(Ca_{0.7}Ce_{0.1}Sr_{0.02}Nd_{0.05})(Ti_{0.9}Al_{0.05}Mo_{0.02})O_3$

Elemental compositions were determined by using an assumption of a total of 8 cations on the Al- and Ti-sites for hollandite, a total of 4 cations on the Ca-, Zr-, and Ti-sites for zirconolite and 1 cation on the Ti-site for perovskite. Further detail regarding the compositions of the various phases is provided in Table 4. The metal

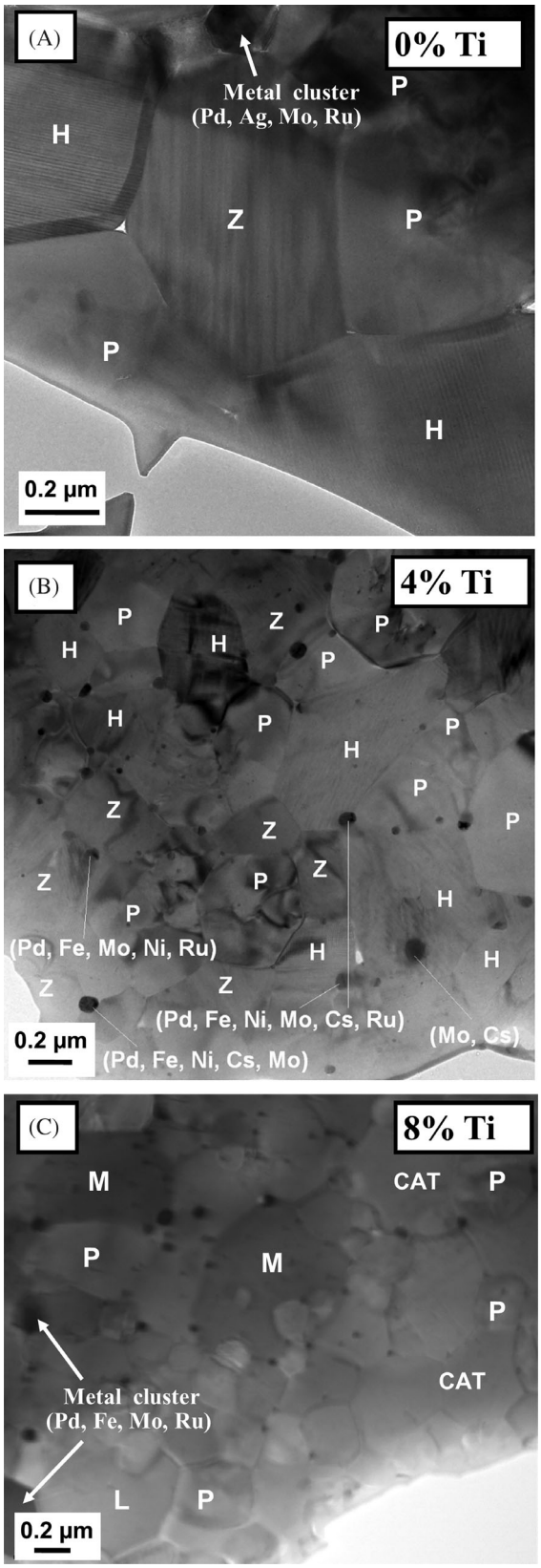

FIGURE 5 Transmission electron microscopy (TEM) bright field images showing the morphology of the (A) 0, (B) 4, and (C) 8 wt.% Ti addition samples. (Z: zirconolite, H: hollandite, P: perovskite, magnetoplumbite-type phases CAT: $Ca(Al,Ti,Zr,Cr)_{12}O_{19}$, M: $Ba(Al,Ti,Fe,Zr,Mo)_{12}O_{19}$ and L: loveringite.

cluster/metallic alloys containing Mo, Pd, Ru and Ag (Fe,Ni) etc. were also observed using microscopic analysis and these clusters were also reported in previous literature.[3] The average elemental partitioning for the different phases is summarised in Table 4 and were as expected.

Ba-hollandite remains a major phase for the sample with 0 wt.% Ti as shown in the XRD pattern, although Cs was detected on average in only ~1 in every 5 grains analyzed via TEM-EDS. The Cs content of hollandite for this sample varied from 0–0.2 f.u., with an average content of 0.05 f.u., as reported in Table 4. As no Ti metal was added in the 0 wt.% Ti sample, the predominant presence of Ti^{4+} is expected in the hollandite structure. In the absence of Ti^{3+}, Cs substitution for Ba on the A-site of the hollandite structure appears limited per unit cell.[27,28] This may be a result of the relatively smaller Al^{3+} ions ($r = 0.585$ Å) on the B site being insufficient in size to allow complete incorporation of the larger Cs ions ($r = 1.75$ Å) into the tunnels of the hollandite structure.[27,28] Therefore, Cs in the 0 wt.% Ti sample was not incorporated into hollandite but formed a metastable phase. Preliminary SEM-EDS analysis confirmed the presence of Cs and Mo on the top altered layer of the monolith (Figure S2), which was captured after a few days of synthesis. This indicates a potentially mobile/soluble form of Cs and Mo (such as, Cs-molybdate), the molybdate form is accessible due to insufficient Ti-metal needed to produce reducing conditions to reduce molybdate to the metallic/alloy form[15] (noting calcination of the powder may also affect the reducing environment). Detailed analysis of the migrated Cs and Mo bearing compounds were not conducted as it was out of the scope of the current study.

At the other end of the redox scale for this set of samples, the sample with 8 wt.% Ti metal showed no evidence in the XRD pattern or SEM and TEM analyses for the Cs-host phase, hollandite. The hollandite structure appeared destabilised by the highly reducing conditions within the HIP canister at this level of Ti metal addition. At this point the mechanism for the destabilisation of hollandite under such reducing conditions is not well understood, however it is likely related to the excess amounts of Ti^{3+} in the structure relative to Ti^{4+}. In the absence of a host phase for Cs, it is free to migrate. It is therefore clear that both insufficient and excessive reducing conditions within the HIP canister during HIP processing will not produce the appropriate Synroc-C phase assemblage required to immobilise Cs, which is known to be a highly chemically reactive and radioactive species present in nuclear wastes.

TEM-EDS analysis of the 8 wt.% Ti sample showed evidence for new phases: magnetoplumbite-type (with varying chemistry) and loveringite phases. With hollandite and zirconolite both destabilised under highly reducing

conditions, Ba^{2+}, Al^{3+}, Ti^{3+}, Zr^{4+} Cs^{+} and Ca^{2+} etc. ions are available to react and form magnetoplumbite-type phase, loveringite and other phases. The magnetoplumbite-type phase was observed with different chemical composition: calcium alumino-titanate (CAT) with nominal composition as ~$Ca(Al,Ti,Zr,Cr)_{12}O_{19}$ (Table S2) was determined from TEM-EDS. Such a CAT phase (hibonite, $CaAl_{12}O_{19}$)[29] was reported previously during Synroc-C production.[30] Another magnetoplumbite-type phase of composition ~$Ba(Al,Ti,Fe,Zr,Mo)_{12}O_{19}$ (Table S2) was also evident in agreement with XRD data (Figures 2 and 3). The co-existence of magnetoplumbite-type phases with Synroc-C phases of hollandite, perovskite, zirconolite have been previously reported.[31] In addition, the composition of selected grains matched that of loveringite, $(CaSrNd)_1(Ti, Al, Fe, Zr, Mo, Ag)_{21}O_{38}$ (Table S2), which was also evident in the XRD data (Figure 2). Again, the presence of loveringite in similar compositions under reducing conditions was reported previously.[32] The TEM-EDS analysis also showed evidence for phases rich in Cs and Mo (Table S2) in the 8 wt.% Ti sample, although it was not possible to confirm the identity of these phases from the XRD and EDS data. In separate work, the formation of $CaTiO_3$ and such calcium aluminate phases have been observed previously when undertaking reactions of $CaCO_3$ and Al_2O_3 with Ti powder.[33]

The redox conditions and the speciation of each element of this study with different Ti metal additions were further investigated via a theoretical study. Each were calculated considering Ellingham diagrams,[34] total oxygen atomic balance and oxygen fugacity data from literature (whenever data at 1250°C was not available, extrapolated numbers were used). For this theoretical analysis, it was also assumed that (i) all oxygen in the wasteform came from the initial oxide precursors only, and (ii) redox conditions of the wasteform reached thermodynamic equilibrium during HIP processing. The reduction of Ru, Pd, Ni and Ag oxides to metal are expected to occur during the calcination step in the reducing environment of N_2-3.5%H_2 at 750°C. Partial reduction of Fe_2O_3 to FeO, and MoO_3 to MoO_2 by H_2 were also expected during calcination and reported previously.[35,36] The presence of bright metal alloy clusters in Figure 4 for the 0 wt.% Ti sample is in agreement with these expectations, for example reduction of PbO and RuO_2 with H_2 during calcination without requiring the addition of Ti metal. However, residual amounts of these oxides may occur due to atmospheric oxygen leakage in the calciner furnace. The calculated theoretical redox environment of HIPed Synroc-C with varying Ti addition is shown in Table S1. For the 0 wt.% Ti sample, the redox environment is likely to be controlled by the presence of MoO_2, which has equilibrium oxygen fugacity of ~10^{-10} atm.[37] Fe^{2+} is also present, and likely to contribute to the redox equilibrium for this sample, since its value is also similar at ~10^{-11} atm. It is not obvious from literature whether reduction of Cr^{3+} will yield Cr^{2+} or Cr^0 at oxygen fugacity of ~10^{-11} to ~10^{-13} atm[38,39]; therefore it is assumed Cr^{2+} / Cr^0 exists in the 2 wt.% Ti sample. For the 4 and 8 wt.% Ti sample with oxygen fugacity above ~10^{-13} atm, Cr is expected to exist as Cr^0[39] and this is in agreement with TEM-EDS analysis for the 8 wt.% Ti sample which shows the presence of Cr (0.5 at%) in the metal alloy phase (no Cr was detected (TEM-EDS) in the metal alloy phase of the 0 wt.% Ti sample).

Incorporation of 2 wt.% Ti metal showed a drastic effect on the redox equilibrium (Table S1) compared to the sample with no Ti addition. The 2 wt.% Ti was expected to be sufficient to reduce all of the Fe and Mo, as well as convert Ce^{4+} to Ce^{3+}. Based on the calculations, the overall Ti oxidation state was determined to be ~3.94. This corresponds to TiO_2 and the Magnéli phase of $Ti_{12}O_{23}$ being in equilibrium, which takes place at an oxygen fugacity of approx. 10^{-13} atm.[40] The presence of TiO_2 is in agreement with the XRD data (Figure 2) for the 2 wt.% Ti sample. Addition of 4 wt.% Ti further reduces the theoretical Ti average oxidation state to ~3.72, and oxygen fugacity therefore to 10^{-14} atm which corresponds to Ti_7O_{13},[12] and this is not accompanied by any changes in speciation of the other metals. XRD analysis (Figure 2) showed evidence for Ti_3O_5 with a few unidentified peaks which may indicate the presence of a mixture of Ti_7O_{13} and Ti_3O_5 Magnéli phases in this HIPed sample. Finally, the 8 wt.% Ti sample has a calculated theoretical fugacity of <10^{-16}, which corresponds to the Magnéli phase Ti_3O_5,[11] the presence of Ti_3O_5 was already confirmed in 4 wt.% Ti sample. The formation of the CAT type phase (where Ti is mostly as Ti^{3+}) with 8 wt.% Ti also indicates the presence of Magnéli phases to reach a fugacity of <10^{-16} atm.

Even though, the theoretical redox equilibrium is expected to reduce all the Mo for the 4 and 8 wt.% Ti samples, TEM-EDS analysis indicates the incorporation of a small portion of the Mo inventory into the Synroc-C phases hollandite and perovskite (Table 4), therefore suggesting the presence of Mo^{4+}. This could be attributed to the preceding diffusion of these ions into the solid solution of these stable phases before the final reducing conditions were achieved at 1250°C.

Increasing Ti metal addition across the sample series increases the availability of Ti^{3+} for possible substitution with other M^{3+} cations within the Synroc-C phases.[7] In hollandite for example, the Al^{3+} can be substituted by Ti^{3+} or Cr^{3+}/Fe^{3+} cations.[9] As such, for the 4 wt.% Ti sample, the partial substitution of Al^{3+} by Ti^{3+} was confirmed by the elemental distribution (see Table 4), and this is in agreement with the increased unit cell parameters of hollandite from XRD results (see Table 3). The average Al

content in hollandite for the 0 wt.% Ti sample was determined to be 1.25 f.u. and this was found to be significantly lower for the 4 wt.% Ti sample at 0.55 f.u. Correspondingly, the Ti content was notably higher for the 4 wt.% Ti sample (7.0 f.u.) relative to the 0 wt.% Ti sample (6.25 f.u.) following Ti^{3+} substitution for Al^{3+}. Partial substitution of Al^{3+} (ionic radius of 0.535 Å in 6-fold coordination[41]) with larger trivalent cations Ti^{3+} (ionic radius of 0.67 Å in 6-fold coordination[41]) is possible and this distorts the tunnel structure and facilitates the incorporation of larger Cs ions[42] in the A site of Ba-hollandite. Thus, hollandite was retained with up to 4 wt.% Ti metal addition via partial cationic substitution. Cations of both Fe and Cr were largely absent from the hollandite structure for the sample with 4 wt.% Ti added, in line with theoretical oxidation states of zero for these elements and their observed presence within the alloy phase.

The rare earth elements Gd, Nd and Ce as well as Y were incorporated into zirconolite by design and as detailed in Table 4. Both Ca and Zr sites in zirconolite are capable of incorporating trivalent REE elements and actinides; however due to the larger polyhedral volume of CaO_8 (21.3 $Å^3$) than ZrO_7 (15 $Å^3$), the larger trivalent REE cations such as, Nd and Gd are expected to be predominantly partitioned on the Ca-site.[43] Charge balance can be maintained by substituting, for example, Ti^{3+} into the Zr site as per the formula $Ca_{1-x}REE_x\ Zr_{1-x}Ti_x\ Ti_2\ O_7$[24,43] or Al^{3+} into the Ti^{4+} site as per $Ca_{1-x}REE_x\ ZrTi_{2-x}\ Al_x\ O_7$ for 3+ REE. The incorporation of Ti^{3+} into zirconolite appears to be limited as demonstrated through studies on single-phase zirconolite where under highly reducing conditions zirconolite is destabilised with partial reduction of Ti^{4+} to Ti^{3+}.[24] This increases the availability of Ca and Ti which react to form perovskite as a secondary phase.[24] Again, although Fe was incorporated into the zirconolite structure for the 0 wt.% Ti sample, it was absent for the 4 wt.% Ti sample similarly to hollandite. In the highly reducing environment established within the HIP canister for the 8 wt.% Ti sample, the newly formed magnetoplumbite- and loveringite-type phases (Table S2) result from destabilisation of both hollandite and zirconolite and the increased availability of Ca, Ba, Ti, Zr, and Al.

For perovskite, the elemental composition appeared to be almost unchanged for all samples studied, irrespective of the redox conditions within the HIP canister, thus demonstrating the stability of this phase under such reducing conditions. Ce, Nd, and Sr were incorporated into the perovskite structure as detailed in Table 4. Sr^{2+} directly substitutes for Ca^{2+} due to their similar ionic radii (ionic radius of 1.44 Å (Sr^{2+}) and 1.34 Å (Ca^{2+}) and in 12-fold coordination) and valence, however Nd^{3+} requires charge compensation. Similarly, Ce incorporation requires charge compensation and could exist as either Ce^{3+} or Ce^{4+} (ionic radius of 1.34 Å (Ce^{3+}) and 1.14 Å (Ce^{4+}) in 12-fold coordination). However, previous studies investigating Ce incorporation into perovskite did not show any evidence of Ce^{4+} under reducing conditions.[44] Therefore, Ce^{3+} is expected in the 4 and 8 wt.% Ti samples. Gd was also present in perovskite (Table 4) and Gd^{3+} substitution for Ca^{2+} was previously reported.[45] All these trivalent REEs can be partitioned in 12 coordinated Ca^{2+} via charge compensation with Al^{3+} on the Ti^{4+} site ($Ca^{2+} + Ti^{4+} \leftrightarrow REE^{3+} + Al^{3+}$) as evidenced in the elemental compositions for the perovskite phase (Table 4). Charge compensation of perovskite by Ti^{3+} (ionic radius of 0.67 Å in 6-fold coordination[41]) is also possible under reducing conditions and has been reported previously to a limited extent.[43,45] This latter charge compensation mechanism may be particularly relevant for the 8 wt.% Ti sample. Trace amounts of both Zr^{4+} and Mo^{4+} (ionic radius of 0.72 Å and 0.65 Å in 6-fold coordination, respectively[41]) were also observed in perovskite for the 8 wt.% Ti sample, as shown in Table 4.

Cr, Ba, and Cs were not incorporated into the perovskite or zirconolite phases, rather preferring to form hollandite or metal alloy phases, by design. Mo was also not observed in the zirconolite phase at all, though minor amounts were measured in the perovskite and hollandite phases when Ti metal was included in the sample. Mo was added as Mo^{6+}, which was expected to be reduced to Mo^{4+} or the metallic state under the reducing conditions provided following addition of Ti metal. As such, Mo was predominantly observed in the metal alloy phases, though Mo^{4+} could also potentially substitute with Ti^{4+}, which is consistent with the observation of Mo in the hollandite/Ti-rich phases (Table 4). In general, the partitioning of elements in the various phases was in accordance with previous literature.[4]

3.3 | TEM and selected area electron diffraction analysis of Synroc-C with 4 wt.% Ti addition

TEM-EDS maps of the sample with 4 wt.% Ti are shown in Figure 6 and these agree with results from the EDS elemental analysis as shown in Table 4. The morphologies of all phases appear to be similar and in the form of fine equiaxed grains of <1 μm size. Only the metal cluster/ alloys were spherical in shape which infers melting during formation within the experimental conditions. It was confirmed that hollandite, the major phase, consisted of primarily Ba, Al, and Ti, which were homogeneously distributed within the phase. Sr and Nd were preferentially partitioned toward the perovskite phase, while Gd appeared equally distributed across the perovskite and zirconolite phases.

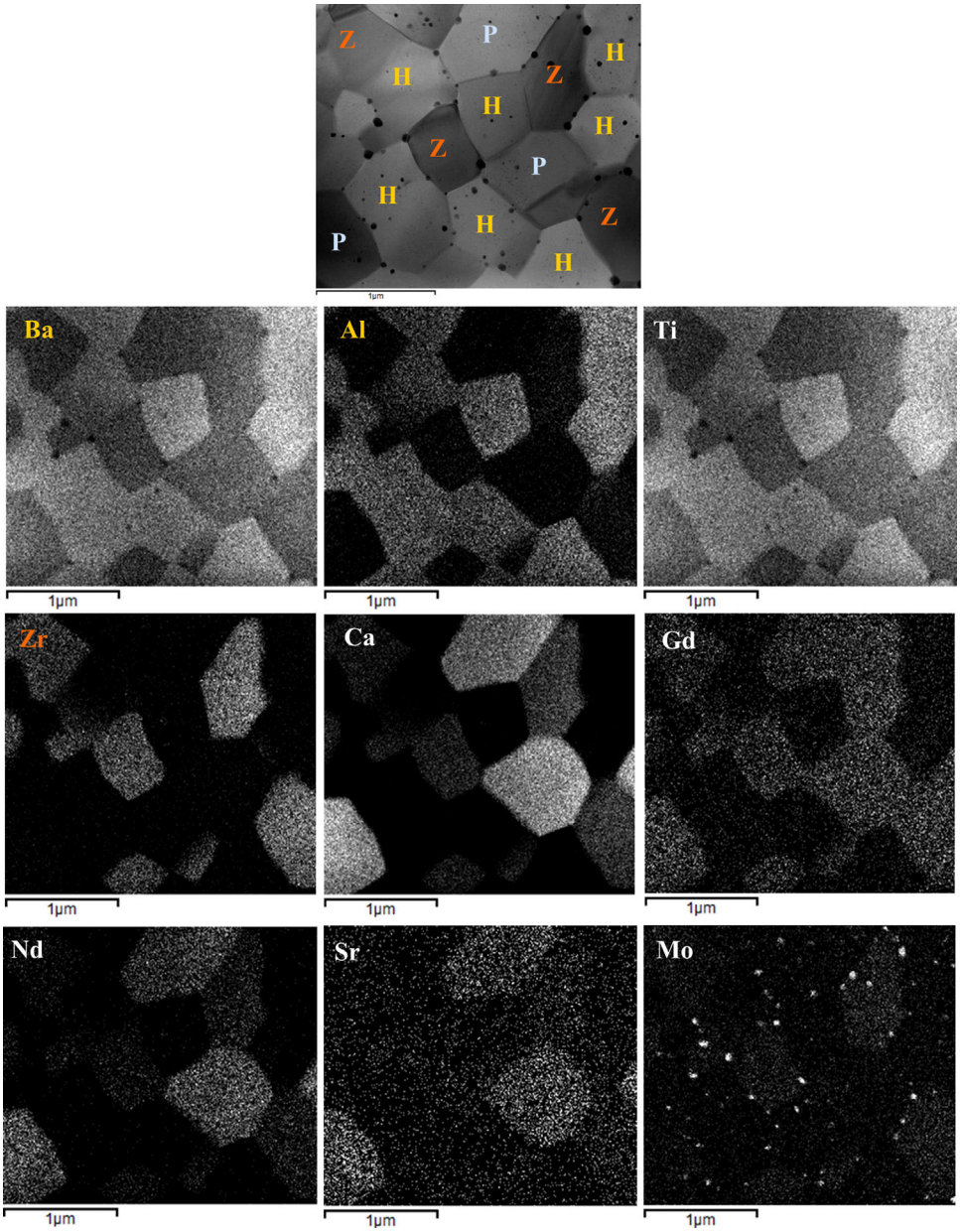

FIGURE 6 Scanning transmission electron microscopy (STEM)-energy dispersive X-ray spectroscopy (EDS) mapped images of Synroc-C sample with 4% Ti metal addition showing elemental distribution in Synroc-C phases. Top image is the STEM image with corresponding individual elemental EDS maps displayed below the STEM image. (Z: zirconolite, H: hollandite, P: perovskite).

This is in agreement with previously reported work.[14] For the 4 wt.% Ti sample, Mo was strongly partitioned toward the alloy phase (Figure 6).

The TEM bright field and high-resolution (HR)-TEM images along with selected area electron diffraction (SAED) images are shown in Figure 7. Small grains of ~100–500 nm size for each phase were found while lattice fringes were evident for the hollandite phase, even at lower magnification (Figure 7). While EDS analysis was used to determine the composition of the different mineral phases, SAED allowed confirmation of crystal structure (Figure 7). Diffraction patterns were matched with the respective expected crystal structures for each phase; in Figure 7 (P) shows perovskite viewed down zone axis [0 1 2] based on space group $P2_1/m$, (H) shows hollandite viewed down zone axis [1 0 2] based on space group $I4/m$, and (Z) shows zirconolite viewed down zone axis [−2 9 5] based on space group $C2/c$.

Further, higher resolution TEM images of the perovskite-hollandite-zirconolite grain boundary region from Figure 7 show lattice contrast from each of the grains indicative of their crystalline nature while also showing some of the spherical metallic alloy inclusions which are seen to be tens of nm in diameter.

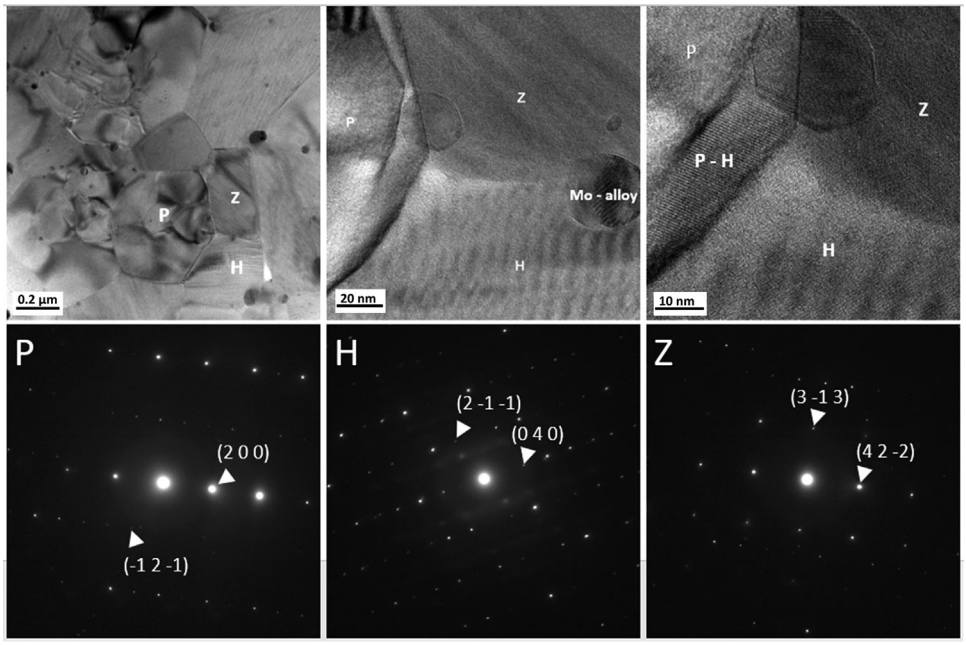

FIGURE 7 Bright field transmission electron microscopy (TEM) and HR-TEM images (Top) with investigated grain highlighted and selected area electron diffraction patterns (SAED) of the phases of the Synroc-C sample with 4 wt.% Ti metal addition. (Z: zirconolite, H: hollandite, P: perovskite).

TABLE 5 Normalised elemental mass loss (NL_i, g m^{-2}) values for Synroc-C with various Ti metal additions from the present work in comparison with previously reported Synroc-C.

Element	Synroc-C[1]	Synroc-C[2]	0 wt.% Ti	2 wt.% Ti	4 wt.% Ti	8 wt.% Ti
Al	0.28	0.28	2.49 ± 0.06	0.066 ± 0.036	0.8 ± 2.5	7.3 ± 1.8
Ca	0.119	0.182	0.837 ± 0.012	0.058 ± 0.037	0.07 ± 0.18	0.033 ± 0.030
Ti	0.0014	0.0014	0.000846 ± 0.000017	0.0013 ± 0.0012	0.0012 ± 0.0017	0.0037 ± 0.0034
Sr	0.147	0.28	3.44 ± 0.21	0.05 ± 0.07	0.066 ± 0.033	0.018 ± 0.016
Zr	0.014	0.168	0.00028 ± 0.00001	0.0004 ± 0.0005	0.0006 ± 0.0010	0.0059 ± 0.0045
Mo	Not reported	3.36	55.4 ± 0.7	1.3 ± 1.3	0.618 ± 0.043	21 ± 8
Cs	0.469	0.924	479 ± 24	0.6 ± 0.9	0.8 ± 1.5	1330 ± 220
Ba	0.476	1.008	1.71 ± 0.12	0.08 ± 0.10	0.064 ± 0.018	0.0003 ± 0.0008
Ce	Not reported	Not reported	0.008 ± 1.680	0.002 ± 0.003	0.0028 ± 0.0045	0.0025 ± 0.0039

[1]21.5 wt.% PW-4b waste loading. Results obtained using the MCC-1 test method with deionised water at 90°C for 7 days (equivalent to ASTM C1220-21, Reference Test Matrix A).[3]

[2]10 wt.% PW-4b waste loading. Results obtained using the MCC-1 test method with deionised water at 90°C for 28 days (equivalent to ASTM C1220-21, Reference Test Matrix B).[3]

3.4 | Wasteform durability

The results of the durability testing for the four HIPed samples are summarized in Table 5, along with durability test results for Synroc-C taken from previous studies. The 0 wt.% Ti sample showed higher normalized elemental mass losses for Al, Ca, Cs, Mo and Sr as compared to previous studies on Synroc-C, as well as in comparison to the 2 and 4 wt.% Ti samples in the current study. In particular, Cs and Mo releases were significantly higher for the 0 wt.% Ti sample, confirming the need for reducing conditions within the HIP canister during wasteform consolidation and the vital role of Ti metal addition to control redox conditions. The high releases of Cs and Mo for the 0 wt.% sample are in line with the observation of water soluble Cs_2MoO_4 in SEM studies, likely formed due to insufficient reducing conditions to incorporate Mo within the metal alloy phase.

At the other end of the scale for this set of samples, the addition of 8 wt.% Ti metal also resulted in high releases of Cs and Mo, along with Al. In this case, destabilisation of the target phases of hollandite and zirconolite has

occurred due to the overly reducing conditions within the HIP canister, and this results in the production of less-durable phases. In the absence of hollandite, which is the highly durable Cs host phase, Cs appears to be associated with an alumino-titanate phase rich in Cs and Mo, as observed via TEM-EDS analysis (Table S2). The presence of this less durable phase results in high release of Cs, Al, and Mo in the dissolution experiment. Surprisingly, Ba release for the 8 wt.% Ti was low and is attributed to its incorporation in the Ba containing magnetoplumbite-type phase.[46] The 2 wt.% Ti and 4 wt.% Ti samples showed improved durability as compared to results reported in the literature and produced a dense and durable multiphase system comprised of the target titanate phases.

4 | CONCLUSIONS

Controlling the redox conditions during consolidation is vital to allow production of a dense and durable Synroc-C wasteform. In the current study, the influence of Ti-metal addition on the redox properties within the HIP canister and its subsequent impact on the quality of the product were examined. Although the target Synroc-C titanate phases of hollandite, zirconolite, perovskite, and rutile were formed without Ti metal addition to the HIP canister prior to HIP consolidation, the resulting material lacked density and showed poor aqueous durability. High elemental mass loss values were measured for this material in durability testing, particularly for Cs and Mo, and evidence suggested the formation of water soluble Cs_2MoO_4. Ti metal addition to the HIP canister at levels of 2 and 4 wt.% produced the target Synroc-C composition with incorporation of the waste elements into the various phases as previously published. The XRD patterns showed a systematic shift toward lower angles in the pattern for those peaks assigned to hollandite as a result of increased Ti metal addition. This shift was attributed to an increase in the unit cell parameters (a and c) of hollandite due to substitution of Al^{3+} with the larger Ti^{3+} cation following Ti metal addition.

After addition of 8 wt.% Ti, both the Synroc-C phases of hollandite and zirconolite were completely destabilised resulting in more complex phase assemblages with only perovskite remaining from the targeted Synroc-C phase assemblage. This sample was also significantly less durable than both the 2 and 4 wt.% Ti samples.

The results demonstrate that the production of dense and durable Synroc-C via the Synroc Technology is highly feasible, and the necessary redox conditions required within the HIP canister can be controlled through Ti metal addition. In the current study, the addition of 2 to 4 wt.% Ti appeared to be optimal for density, phase formation, and aqueous durability.

ACKNOWLEDGMENTS

The authors thank I. Watson and I. Kurlapski for assistance with sample preparation, N. Webb for HIPing, I. Chironi for TG analysis and Nuclear Science and Technology (NST) at ANSTO for material characterizations.

Open access publishing facilitated by Australian Nuclear Science and Technology Organisation, as part of the Wiley - Australian Nuclear Science and Technology Organisation agreement via the Council of Australian University Librarians.

CONFLICT OF INTEREST STATEMENT

The authors declare that they have no known competing financial interests or personal relationships that could have appeared to influence the work reported in this paper.

ORCID

Rifat Farzana https://orcid.org/0000-0001-8611-8744
Pranesh Dayal https://orcid.org/0000-0002-7324-5258
Robert D. Aughterson https://orcid.org/0000-0002-1704-024X
Pramod Koshy https://orcid.org/0000-0003-0282-5535
Daniel J. Gregg https://orcid.org/0000-0003-4703-7217

REFERENCES

1. Ringwood A, Kesson SE, Ware NG, Hibberson W, Major A. Immobilisation of high level nuclear reactor wastes in SYNROC. Nature. 1979;278(5701):219–23.
2. Gregg DJ, Farzana R, Dayal P, Holmes R, Triani G. Synroc technology: perspectives and current status. J Am Ceram Soc. 2020;103(10):5424–41.
3. Ringwood A, Kesson S. SYNROC from radioactive waste forms from the future. In: Lutze W, Ewing RC, editors. Radioactive waste forms for the future. Amsterdam, Netherlands: North-Holland Press; 1988. p. 233–334.
4. Gregg DJ, Vance ER. Synroc tailored waste forms for actinide immobilization. Radiochim Acta. 2017;105(11):907–25.
5. Gregg DJ, Vance ER, Dayal P, Farzana R, Aly Z, Holmes R, et al. Hot Isostatically Pressed (HIPed) fluorite glass-ceramic wasteforms for fluoride molten salt wastes. J Am Ceram Soc. 2020;103(10):5454–69.
6. Vance E, Gregg DJ, Grant C, Stopic A, Maddrell ER. Silver iodide sodalite for 129I immobilisation. J Nucl Mater. 2016;480:177–81.
7. Oversby V. Properties of SYNROC C nuclear-waste form: a state-of-the-art review. Livermore, CA: Lawrence Livermore National Lab.; 1982.
8. Ringwood TJAS. Immobilization of radioactive wastes in SYNROC: a high-performance titanate ceramic waste form composed of minerals that have survived in various natural environments for long periods, SYNROC should permit safe burial of waste in deep drill holes. Am Sci. 1982;70(2):201–7.

9. Ringwood A. Disposal of high-level nuclear wastes: a geological perspective. Mineral Mag. 1985;49(351):159–76.
10. Perera D, Begg BD, Vance ER, Stewart MWA. Application of crystal chemistry in the development of radioactive wasteforms. Advances in Technology of Materials and Materials Processing Journal. 2004;6:214–7.
11. Brooks K., Native iron: Greenland's natural blast furnaces. Geol Today. 2015;31(5):176–80.
12. Walsh F, Wills R., The continuing development of Magnéli phase titanium sub-oxides and Ebonex® electrodes. Electrochim Acta. 2010;55(22):6342–51.
13. Zhao P-f, Li W, LI G, Cheng P, Pang Z, Xiong X, et al. Progress in Ti3O5: synthesis, properties and applications. Transactions of Nonferrous Metals Society of China. 2021;31(11):3310–27.
14. Lumpkin GR, Smith KL, Blackford MG., Partitioning of uranium and rare earth elements in Synroc: effect of impurities, metal additive, and waste loading. J Nucl Mater. 1995;224(1):31–42.
15. Kesson S., Immobilization of cesium in SYNROC hollandite. Radioact. Waste Manage. Nucl. Fuel Cycle; (United Kingdom). 1983;4(1):53–72.
16. Ryerson FJ., Phase equilibria of nuclear waste ceramics: the effect of oxygen fugacity. J Am Ceram Soc. 1984;67(2):75–82.
17. Stewart MWA, Begg BD, Day RA, Moricca S, Vance ER, Walls PA. Low-risk alternative waste forms for actinide immobilization. In: Proceedings of the Annual Waste Management Symposium (WM'05). February 27–March 3, 2004. Tucson, AZ; 2005.
18. Ringwood A, Major A, Ramm EJ, Padgett J. Uniaxial hot-pressing in bellows containers. Nuclear and chemical waste management. 1983;4(2):135–40.
19. Carter M, Stewart M, Leung S. Microstructures of inactive SYNROC-C samples produced by different hot-consolidation methods. Westerville, OH: American Ceramic Society; 1996.
20. Clark B, Tumurugoti P, Sundaram SK, Amoroso JW, Marra JC, Brinkman KS. Microstructures of melt-processed and spark plasma sintered ceramic waste forms. Metallurgical and Materials Transactions E. 2014;1(4):341–8.
21. ASTM International. ASTM C1220-21 standard test method for static leaching of monolithic waste forms for disposal of radioactive waste. West Conshohocken, PA: ASTM International; 2021. https://doi.org/10.1520/C1220-21
22. Ellison SL, Williams A. Eurachem/CITAC guide: quantifying uncertainty in analytical measurement. 3rd ed.
23. Ringwood A. Progress report: Immobilization of sodium and phosphorus-bearing PW-7a waste in SYNROC. Canberra, Australia: Australian National University Research School of Earth Sciences; 1982.
24. Begg B, Vance ER, Hunter BA, Hanna JV. Zirconolite transformation under reducing conditions. J Mater Res. 1998;13(11):3181–90.
25. Farzana R, Zhang Y, Dayal P, Aly Z, Holmes R, Triani G, et al. Pyrochlore glass-ceramics for the immobilization of molybdenum-99 production wastes: demonstrating scalability and flexibility to waste stream variance. J Eur Ceram Soc. 2021;41(14):7269–81.
26. Tumurugoti P, Clark BM, Edwards DJ, Amoroso J, Sundaram SK. Cesium incorporation in hollandite-rich multiphasic ceramic waste forms. J Solid State Chem. 2017;246:107–12.
27. Xu Y, Feygenson M, Page K, Nickles LS, Brinkman KS. Structural evolution in hollandite solid solutions across the A-site compositional range from Ba1. 33Ga2. 66Ti5. 34O16 to Cs1. 33Ga1. 33Ti6. 67O16. J Am Ceram Soc. 2016;99(12):4100–6.
28. Aubin-Chevaldonnet V, Caurant D, Dannoux A, Gourier D, Charpentier T, Mazerolles L, et al. Preparation and characterization of (Ba, Cs)(M, Ti) 8O16 (M = Al3+, Fe3+, Ga3+, Cr3+, Sc3+, Mg2+) hollandite ceramics developed for radioactive cesium immobilization. J Nucl Mater. 2007;366(1-2):137–60.
29. Li Y, Zhao H, Yang Y, Feng Z, Zhang H, Yu J, et al. The restructuring-sintering mechanism of calcium aluminotitanate in tundish permanent lining castables. Ceram Int. 2020;46(18):29282–9.
30. Sobolev I, Stefanovsky SV, Omelianenko BI, Ioudintsev SV, Vance ER, Jostsons A. Comparative study of Synroc-C ceramics produced by hot-pressing and inductive melting. MRS Online Proceedings Library Archive. 1996;465:371–8.
31. Ringwood A. Investigations on SYNROC mineralogy. Progress report. CA, Livermore: Lawrence Livermore National Lab.; 1982.
32. Dayal P, Farzana R, Zhang Y, Lumpkin GR, Holmes R, Triani G, et al. Profiling hot isostatically pressed canister–wasteform interaction for Pu-bearing zirconolite-rich wasteforms. J Am Ceram Soc. 2022;105(8):5359–72.
33. Miranda-Hernández JG, Vargas-Hernández J, Casarrubias-Vargas H, González-Morán CO, Refugio-García E, Flores Cuautle J de JA. Synthesis and effect of CaTiO3 formation in CaO· Al2O3 by solid-state reaction from CaCO3· Al2O3 and Ti. Mater Chem Phys. 2019;232:57–64.
34. Ellingham diagrams. web.mit.edu. https://web.mit.edu/2.813/www/readings/Ellingham_diagrams.pdf. Accessed 1 Aug 2022.
35. Dang J, Zhang G-H, Chou K-C, Reddy RG, He Y, Sun Y. Kinetics and mechanism of hydrogen reduction of MoO3 to MoO2. Int J Refract Met Hard Mater. 2013;41:216–23.
36. Zieliński J, Zglinicka I, Znak L, Kaszkur Z. Reduction of Fe2O3 with hydrogen. Appl Catal, A. 2010;381(1-2):191–6.
37. Myhill R, Ojwang DO, Ziberna L, Frost DJ, Ballaran TB, Miyajima N. On the P–T–fO_2 stability of Fe_4O_5, Fe_5O_6 and Fe_4O_5-rich solid solutions (vol 171, 51, 2016). Contrib Mineral Petrol. 2018;173(1). https://doi.org/10.1007/s00410-016-1258-4
38. Griffin WL, Gain SEM, Saunders M, Cámara F, Bindi L, Spartà D, et al. Cr2O3 in corundum: ultrahigh contents under reducing conditions. American Mineralogist: Journal of Earth and Planetary Materials. 2021;106(9):1420–37.
39. Mittal A, Albertsson GJ, Gupta GS, Seetharaman S, Subramanian S. Some thermodynamic aspects of the oxides of chromium. Metallurgical and Materials Transactions B. 2014;45(2):338–44.
40. Pedersen A, RØnsbo J., Oxygen deficient Ti oxides (natural magnéli phases) from mudstone xenoliths with native iron from Disko, central West Greenland. Contrib Mineral Petrol. 1987;96(1):35–46.
41. Shannon RD., Revised effective ionic radii and systematic studies of interatomic distances in halides and chalcogenides. Acta Crystallogr, Sect A. 1976;32(5):751–67.
42. Tumurugoti P, Sundaram SK, Misture ST, Marra JC, Amoroso J. Crystallization behavior during melt-processing of ceramic waste forms. J Nucl Mater. 2016;473:178–88.

43. Fielding P, White T., Crystal chemical incorporation of high level waste species in aluminotitanate-based ceramics: valence, location, radiation damage, and hydrothermal durability. J Mater Res. 1987;2(3):387–414.
44. Begg B, Vance E, Lumpkin G., Charge compensation and the incorporation of cerium in zirconolite and perovskite. MRS Online Proceedings Library (OPL). 1997;506:79–86.
45. Vance E, Day RA, Zhang Z, Begg BD, Ball CJ, Blackford MG. Charge compensation in Gd-doped CaTiO3. J Solid State Chem. 1996;124(1):77–82.
46. Harker A, Morgan PED, Clarke DR, Flintoff JJ, Jantzen CM. Formulation and processing of alumina based ceramic nuclear waste forms. Allegan, MI: Rockwell International Science Center; 1983.

SUPPORTING INFORMATION

Additional supporting information can be found online in the Supporting Information section at the end of this article.

How to cite this article: Farzana R, Dayal P, Peristyy A, Sutton P, Aly Z, Aughterson RD, et al. Effect of Ti-metal addition on hot-isostatically pressed (HIPed) Synroc-C. J Am Ceram Soc. 2023;106:6971–6986.
https://doi.org/10.1111/jace.19313